

# Image Super Resolution via Bilinear Pooling: Application to Confocal Endomicroscopy

Saeed Izadi, Darren Sutton, and Ghassan Hamarneh

School of Computing Science, Simon Fraser University, Canada  
{saeedi, darrens, hamarneh}@sfu.ca

**Abstract.** Recent developments in image acquisition literature have miniaturized the confocal laser endomicroscopes to improve usability and flexibility of the apparatus in actual clinical settings. However, miniaturized devices collect less light and have fewer optical components, resulting in pixelation artifacts and low resolution images. Owing to the strength of deep networks, many supervised methods known as super resolution have achieved considerable success in restoring low resolution images by generating the missing high frequency details. In this work, we propose a novel attention mechanism that, for the first time, combines 1st- and 2nd-order statistics for pooling operation, in the spatial and channel-wise dimensions. We compare the efficacy of our method to 11 other existing single image super resolution techniques that compensate for the reduction in image quality caused by the necessity of endomicroscope miniaturization. All evaluations are carried out on three publicly available datasets. Experimental results show that our method can produce competitive results against state-of-the-art in terms of PSNR, SSIM, and IFC metrics. Additionally, our proposed method contains small number of parameters, which makes it lightweight and fast for real-time applications.

## 1 Introduction

Colorectal cancer is known as the fourth most-common cancer and remains one of the leading causes of cancer related mortality in the world. In 2018, more than 1 million people were affected by colorectal cancer worldwide, resulting in an estimated 55,000 deaths [3]. Rapid histopathologic assessment is an important tool that may improve disease prognosis by detecting early-stage cancer and pre-cancerous conditions. Although biopsy and *ex-vivo* tissue examination are widely accepted as the diagnostic gold standard, such procedures take time and may limit the ability of the endoscopist to rapidly gauge disease severity. Confocal laser endomicroscopy (CLE), on the other hand, has substantially improved real-time *in-vivo* visualization of the subsurface of living cells, vascular structures, and tissue patterns during endoscopic examination [11].

For *in-vivo* histological examination, the large size of the microscope complicates navigation of the interior of the body in a clinical setting. Therefore, it is necessary to reduce the size of the microscope to completely and safely access the organ(s) of interest. However, miniaturization reduces the number of optical elements in the microscope probe, introducing pixelation artifacts in the acquired images. One strategy to remove image artifacts and enhance image quality is to directly post-process degraded images. An emerging process in the field of image processing, referred to as single image super-resolution (SR), aims to reconstruct an accurate high-resolution (HR) image given its low-resolution (LR) counterpart. Thus, SR is a promising software method to mitigate image degradation due to hardware miniaturization.

In this paper, we present a lightweight convolutional neural network (CNN) that is appropriate for frame-wise SR by incorporating novel attention mechanisms. We implement attention using the Squeeze-and-Excitation network unit first reported by Hu et al. [8], resulting in improved training efficiency and adaptability of learned features. Our attention modules are based on a combination of 1<sup>st</sup>-order pooling and 2<sup>nd</sup>-order pooling (a.k.a. bilinear pooling), improving the quality of learned features in the network by considering pairwise correlations along feature channels and spatial regions [6]. The compactness and computational speed of our network lend well to real-time implementation during *in-vivo* examination. Additionally, our network has a reduced number of learning parameters, which is an important advantage when dealing with small datasets commonly found in biomedical applications. We demonstrate that stacking attention modules in the middle of a low-level feature extraction head and a feature integration tail quantitatively and qualitatively produces competitive results against existing SR methods and generalizes well over unseen microscopic datasets.

## 2 Related Works

**Image Super Resolution.** Among traditional SR algorithms, Huang et al. [9] proposed leveraging self-similarity modulo affine transformations to accommodate natural deformation of recurring statistical priors within and across scales of an image. Timofte et al. [19,20] used a combination of neighbor embedding and sparse dictionary learning over an external database and proposed anchored neighborhood regression in the dictionary atom space. Recently, CNNs have advanced the SR research field by directly learning the mapping between LR and HR images [5,12,13,14,1]. Dong et al. [5] demonstrated that a fully convolutional network trained end-to-end can perform LR-to-HR nonlinear mapping. Kim et al. [12] suggested a trained network to predict additive details in the form of a residual image, which is summed with the interpolated image. Kim et al. [13] tackled overfitting through reducing the number of parameters by recursive convolutional layers. Lai et al. [14] designed a network which progressively reconstructs the sub-band residuals of high-resolution images at multiple pyramid levels. Ahn et al. [1] improved speed and efficiency of SR models by designing

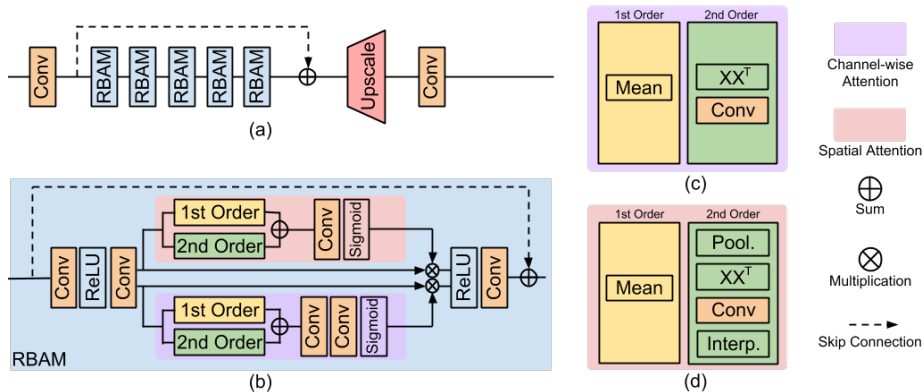


Fig. 1: (a) The overall architecture of our proposed network. (b) RBAM architecture. (c) channel-wise and (d) spatial attention architectures.

a cascade mechanism over residual networks. Lastly, Cheng et al. [4] exploited recursive squeeze and excitation modules in a network to exploit relationships between channels.

**SR for Confocal Endomicroscopy.** Izadi et al. [10] reported the first attempt to deploy CNNs on CLE images. They used a densely connected CNN to transform synthetic LR images into HR ones. Ravi et al. [16] employed a CNN to restore missing details into LR images. They collected a set of consecutive LR frames and generated synthetic HR images using a video registration technique. In a more recent study [17], Ravi et al. trained a CNN for unsupervised SR on CLE images using a cycle consistency regularization, designed to impose acquisition properties on the super-resolved images.

### 3 Method

**Network Overview.** Fig. 1-a depicts the overall architecture of our proposed LR-to-SR network. Let  $I_{LR} \in \mathbb{R}^{1 \times W \times H}$ ,  $I_{SR} \in \mathbb{R}^{1 \times rH \times rW}$ , and  $r$  denote the low resolution input and super-resolved output, and the downsample factor, respectively. We use a convolution layer, denoted by  $\mathcal{F}(\cdot)$ , with a  $3 \times 3$  kernel and  $C$  output channels to extract initial features  $H^0 \in \mathbb{R}^{C \times H \times W}$ , i.e.

$$H^0 = \mathcal{F}_c(I_{LR}; \theta_0), \quad (1)$$

where  $\theta$  refers to the learnable parameters. The initial features  $H^0$  are updated by sequential residual attention modules, denoted as  $\mathcal{G}(\cdot)$  and a skip connection. The entire high-level feature extraction stage is denoted as  $\mathcal{B}(\cdot)$ :

$$H^B = \mathcal{B}(H^0) = \mathcal{G}^b(\mathcal{G}^{b-1}(\dots(\mathcal{G}^1(H^0))\dots)) + H^0. \quad (2)$$

To upsample the feature maps, we use sub-pixel convolutions, denoted as  $\mathcal{U}(\cdot)$ , followed by a single channel  $1 \times 1$  convolution for SR reconstruction:

$$I_{SR} = \mathcal{F}_1(\mathcal{U}(H^B; \theta_{up}); \theta_{rec}). \quad (3)$$

**Residual Bilinear Attention Module.** In RBAM, we combine 1<sup>st</sup>- and 2<sup>nd</sup>-order pooling operations spatially and channel-wise to recalibrate learned features for efficient network training. Fig. 1-b illustrates the structure of our proposed RBAM. Mathematically, we formulate RBAM as:

$$\mathbf{H}^b = \mathcal{G}^b(\mathbf{H}^{b-1}) = \mathcal{Q}^b(\mathbf{H}^{b-1}) + \mathbf{H}^{b-1}, \quad (4)$$

where  $\mathcal{Q}(\cdot)$  denotes the attention modules before the skip connection. Given the input feature maps  $\mathbf{H}^b \in \mathbb{R}^{C \times H \times W}$ , two convolutions with  $3 \times 3$  kernel size interleaved with a ReLU activation function are performed to produce high-level feature maps  $\mathbf{H}_{\text{conv}}^b \in \mathbb{R}^{C \times H \times W}$  as input to the attention branches:

$$\mathbf{H}_{\text{conv}}^b = \mathcal{F}_c(\mathcal{F}_c(\mathbf{H}^{b-1}; \theta_1^b); \theta_2^b). \quad (5)$$

**Channel-wise Attention (CA) Branch.** CA leverages the inter-channel correspondence between feature responses (Fig. 1-c). 1<sup>st</sup>- and 2<sup>nd</sup>-order pooling mechanisms operate on  $\mathbf{H}_{\text{conv}}^b$ , producing two vectors  $\mathbf{F}_{\text{ca}}^{1\text{st}}, \mathbf{F}_{\text{ca}}^{2\text{nd}} \in \mathbb{R}^{C \times 1 \times 1}$ .  $\mathbf{F}_{\text{ca}}^{1\text{st}}$  is the 1<sup>st</sup>-order CA obtained by spatial average pooling to squeeze the feature map of each channel [8]. To obtain 2<sup>nd</sup>-order CA, pairwise channel correlations are computed in the form of a covariance matrix  $\Sigma \in \mathbb{R}^{C \times C}$  by spatial flattening, dimension permutation, and matrix multiplication. Each row in  $\Sigma$  encodes the statistical dependency of a channel with respect to every other channel [6]. Given the covariance matrix  $\Sigma$ , we adopt a row-wise convolution with  $1 \times C$  kernel size to produce the 2<sup>nd</sup>-order CA vector  $\mathbf{F}_{\text{ca}}^{2\text{nd}}$ . Finally, two successive 1-D convolutions interleaved with a ReLU activation function operate on a vector formed by the sum of  $\mathbf{F}_{\text{ca}}^{1\text{st}} + \mathbf{F}_{\text{ca}}^{2\text{nd}}$ . The output of the convolution operation is fed into a sigmoid function  $\sigma$ , followed by element-wise multiplication  $\otimes$  to produce the  $b^{\text{th}}$  updated features maps  $\mathbf{H}_{\text{ca}}^b$ :

$$\mathbf{H}_{\text{ca}}^b = \mathbf{H}_{\text{conv}}^b \otimes \sigma(\mathcal{F}_c(\mathcal{F}_{\frac{1}{4}}(\mathbf{F}_{\text{ca}}^{1\text{st}} + \mathbf{F}_{\text{ca}}^{2\text{nd}}; \theta_3^b); \theta_4^b)). \quad (6)$$

**Spatial Attention (SA) Branch.** SA indicates shared correspondence between spatial regions across all feature maps (Fig. 1-d). Given  $\mathbf{H}_{\text{conv}}^b$  as the input, the 1<sup>st</sup>-order spatial attention matrix,  $\mathbf{F}_{\text{sa}}^{1\text{st}} \in \mathbb{R}^{1 \times H \times W}$ , is computed by the average pooling operation along channel dimension to aggregate information for each spatial location across all features. To compute 2<sup>nd</sup>-order spatial attention matrix,  $\mathbf{F}_{\text{sa}}^{2\text{nd}} \in \mathbb{R}^{1 \times H \times W}$ , we first reduce the spatial size of feature maps to  $H' \times W'$  ( $8 \times 8$  in our implementation) by applying average pooling. Then, appropriate reshaping, dimension permutation and matrix multiplication is adopted to obtain the covariance matrix  $\Sigma \in \mathbb{R}^{H'W' \times H'W'}$ . Similar to channel-wise attention, a row-wise convolution with  $1 \times H'W'$  kernel size is applied on  $\Sigma$ . Eventually, dimension permutation and nearest neighbor interpolation produce  $\mathbf{F}_{\text{sa}}^{2\text{nd}}$ . We add these two matrices together element-wise and apply a convolution with  $1 \times 1$  kernel size that feeds a sigmoid function. Spatial attention is realised by element-wise multiplication over all feature maps, formulated as:

$$\mathbf{H}_{\text{sa}}^b = \mathbf{H}_{\text{conv}}^b \otimes \sigma(\mathcal{F}_c(\mathbf{F}_{\text{sa}}^{1\text{st}} + \mathbf{F}_{\text{sa}}^{2\text{nd}}; \theta_5^b)) \quad (7)$$

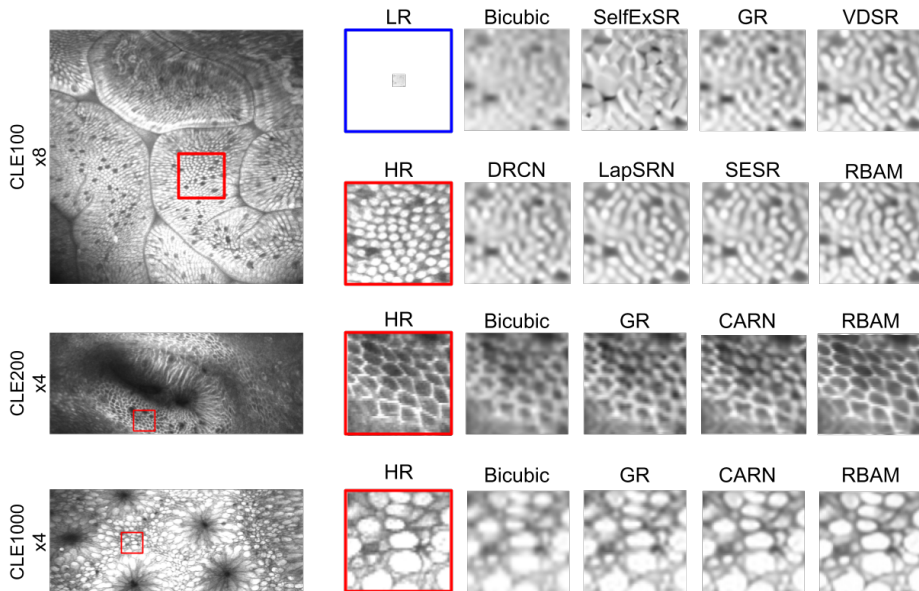


Fig. 2: Qualitative results for image SR at  $\times 4$  and  $\times 8$  scale factors. Each row corresponds to a sample from each dataset, CLE100, CLE200, and CLE1000.

Table 1: Details of the datasets used in our evaluation.

dataset	provided by	#patients	#images	anatomical site	image size
CLE100	Leong et al. [15]	30	181	small intestine	$1024 \times 1024$
CLE200	Grisan et al. [7]	32	262	esophagus	$1024 \times 1024$
CLE1000	Ștefănescu et al. [18]	11	1025	colorectal mucosa	$1024 \times 1024$

**Attention Fusion.** The updated features are concatenated ( $\#$ ) and aggregated via a convolution with kernel  $1 \times 1$  kernel. Lastly,  $H^b$  is added via skip connection:

$$H^b = \mathcal{F}_c(H_{ca}^b \# H_{sa}^b; \theta_6^b) + H^{b-1}. \quad (8)$$

## 4 Results

**Data.** We evaluate existing SR methods, as well as our proposed RBAM, on three publicly available CLE datasets (Table 1), which share similar textural appearances. The comparisons are carried out based on methods’ ability to reconstruct  $1024 \times 1024$  HR image from a synthesized LR counterpart obtained via bicubic downsampling with a factor of  $\times 2$ ,  $\times 4$ , or  $\times 8$ .

**Training Settings.** We train all methods on a random partition (80%) of CLE100, and evaluate them on the remaining 20% as well as CLE200, and CLE1000. For DL-based methods, we replicated the reported training settings, and used public code for traditional algorithms. For our model, we use  $B = 5$  RBAMs and set the number of features to  $C = 64$  to create a lightweight net-

Table 2: PSNR scores for different RBAM configurations on CLE100  $\times 2$  SR.

Attention	CA	1 <sup>st</sup> order	×	✓	×	✓	×	✓
		2 <sup>nd</sup> order	×	×	✓	✓	×	✓
	SA		×	×	×	×	✓	✓
#params			555K	566K	586K	586K	884K	956K
PSNR			38.45	38.52	38.49	38.56	38.48	38.60

work. In each training batch, 16 LR patches of size  $48 \times 48$  are randomly extracted as inputs, and augmented by random  $90^\circ$  rotations and horizontal/vertical flip. We use Adam optimizer and L1 loss to train our network for 300 epochs. Initial learning rate is set to  $10^{-4}$  and is halved every 50 epochs.

**Ablation Investigation.** We discern the effectiveness of the individual components in our network modules by ablating attention blocks and evaluating performance after 50 epochs. Table 2 shows that, for CLE100 at  $\times 2$  SR, attention-based variants outperform the baseline, demonstrating the merits of incorporating spatial and channel-wise contextual information. It is also clear that using both 1<sup>st</sup> and 2<sup>nd</sup>-order pooling operations simultaneously outperform using either 1<sup>st</sup> or 2<sup>nd</sup>-order channel-wise pooling individually. We similarly note that using both spatial and channel-wise attention outperforms either one alone.

**Comparison to State-of-the-art.** We compare the performance of traditional algorithms including ANR [19], GR [19], A+ [20], and SelfExSR [9], as well as DL-based techniques including SRCNN [5], VDSR [12], DRCN [13], LapSRN [14], SESR [4], CARN [1], and our proposed RBAM. Table 3 summarizes the quantitative comparisons in terms of peak signal-to-noise-ratio (PSNR), structural similarity (SSIM), information fidelity criterion (IFC) [21], number of parameters, and inference time at  $\times 2$ ,  $\times 4$ , and  $\times 8$  SR. From the table, we can see that most DL-based methods consistently outperform traditional SR algorithms in PSNR and SSIM metrics. However, traditional algorithms, including GR [20] and A+ [20] exhibit the best IFC scores for  $\times 2$  and  $\times 4$  SR, respectively. This could be explained by artifacts in traditional SR reconstructions rewarded by wavelet filters in the IFC metric. Visual inspection reveals the disparity between IFC scores and the quality of traditional SR reconstructions. This metric has also been shown to anticorrelate with perceived SR reconstruction quality [2]. On the other hand, RBAM does obtain the best IFC scores among DL-based methods, and outperforms the mean PSNR over all datasets by 0.27dB, 0.29dB and 0.14dB for  $\times 2$ ,  $\times 4$  and  $\times 8$  SR, respectively. Furthermore, RBAM is a practical compromise between number of parameters, inference time, and generalization. Lastly, quantitative results point out the weakness of SelfExSR [9] on CLE modality. It however comes at no surprise as SelfExSR uses vanishing points and perspective geometry to expand patch search, which are cues not found in CLE images. Fig. 2 shows selected images from each dataset for qualitative assessment. The first row of Fig. 2, corresponding to  $\times 8$  SR, shows that RBAM can delicately restore high-frequency cues, such as granular textures and cell morphology. The

Table 3: Quantitative results of SR models at  $\times 2$ ,  $\times 4$  and  $\times 8$  factors. **Bold** indicates the best results.  $\clubsuit$  and  $\dagger$  denote traditional and DL-based methods, respectively.

Methods	Scale	CLE100			CLE200			CLE1000			params	time
		PSNR	SSIM	IFC	PSNR	SSIM	IFC	PSNR	SSIM	IFC		
Bicubic		35.15	0.8733	6.989	36.99	0.9045	6.756	35.75	0.9034	6.977		- 0.02
SelfExSR $\clubsuit$ [9]		29.04	0.8909	8.014	28.02	0.9150	7.612	28.40	0.9153	7.994		- 211.
A+ $\clubsuit$ [20]		35.77	0.8991	9.123	37.69	0.9242	8.833	36.35	0.9218	9.132		- 6.72
ANR $\clubsuit$ [19]		38.27	0.9308	11.56	40.60	0.9536	11.32	39.12	0.9502	11.55		- 6.07
GR $\clubsuit$ [19]	$\times 2$	38.40	0.9333	<b>12.01</b>	40.76	0.9547	<b>11.77</b>	39.28	0.9521	<b>12.01</b>		- 4.47
SRCNN $\dagger$ [5]		37.54	0.9245	9.569	39.79	0.9468	9.112	38.32	0.9448	9.519	57K	0.06
VDSR $\dagger$ [12]		38.48	0.9341	10.48	40.71	0.9545	9.915	39.30	0.9524	10.43	666K	0.25
DRCN $\dagger$ [13]		38.43	0.9330	10.40	40.69	0.9543	9.850	39.26	0.9518	10.34	112K	0.48
LapSRN $\dagger$ [14]		38.50	0.9341	10.78	40.79	0.9554	10.25	39.33	0.9525	10.74	435K	0.07
SESR $\dagger$ [4]		38.54	0.9350	10.79	40.80	0.9555	10.25	39.34	0.9527	10.75	312K	0.27
CARN $\dagger$ [1]		38.58	0.9352	10.89	<b>40.82</b>	0.9555	10.33	39.37	0.9529	10.85	962K	0.14
RBAM (Ours) $\dagger$		<b>38.68</b>	<b>0.9369</b>	10.93	40.80	<b>0.9560</b>	10.34	<b>39.44</b>	<b>0.9541</b>	10.90	956K	0.18
<hr/>												
Bicubic		30.82	0.6702	2.367	32.56	0.7388	2.076	31.63	0.7567	2.306		- 0.02
SelfExSR [9]		27.43	0.7017	2.503	27.06	0.7648	2.349	27.20	0.7715	2.625		- 224.
A+ [20]		30.91	0.7111	<b>3.061</b>	32.89	0.7700	<b>2.677</b>	31.74	0.7774	<b>2.919</b>		- 3.03
ANR [19]		31.27	0.7209	2.761	33.28	0.7795	2.642	32.25	0.7901	2.891		- 2.88
GR [19]		31.28	0.7258	2.781	33.31	0.7830	2.655	32.27	0.7931	2.906		- 2.31
SRCNN [5]	$\times 4$	31.45	0.7089	2.750	33.11	0.7685	2.358	32.17	0.7799	2.634	57K	0.06
VDSR [12]		31.60	0.7160	2.861	33.29	0.7758	2.417	32.34	0.7857	2.723	666K	0.25
DRCN [13]		31.68	0.7216	2.903	33.38	0.7799	2.450	32.43	0.7904	2.749	112K	0.48
LapSRN [14]		31.64	0.7198	2.878	33.32	0.7784	2.358	32.38	0.7890	2.773	870K	0.08
SESR [4]		31.79	0.7268	2.937	33.52	0.7855	2.480	32.56	0.7947	2.809	624K	0.33
CARN [1]		31.84	0.7287	2.994	33.54	0.7865	2.515	32.58	0.7955	2.821	1110K	0.06
RBAM (Ours)		<b>31.93</b>	<b>0.7313</b>	3.006	<b>33.72</b>	<b>0.7891</b>	2.530	<b>32.66</b>	<b>0.7973</b>	2.831	1109K	0.07
<hr/>												
Bicubic		28.05	0.5233	0.816	29.92	0.6201	0.674	28.82	0.6585	0.867		- 0.02
SelfExSR [9]		25.73	0.5561	0.760	26.00	0.6590	0.724	25.89	0.6699	0.920		- 228.
A+ [20]		28.16	0.5655	1.014	30.26	0.6506	0.825	29.19	0.6772	1.052		- 1.96
ANR [19]		28.29	0.5650	0.867	30.36	0.6515	0.817	29.38	0.6835	1.049		- 1.91
GR [19]		28.30	0.5654	0.875	30.38	0.6551	0.823	29.39	0.6856	1.060		- 1.61
SRCNN [5]	$\times 8$	28.40	0.5534	0.882	30.25	0.6473	0.726	29.24	0.6759	0.938	57K	0.06
VDSR [12]		28.64	0.5609	1.032	30.49	0.6516	0.804	29.60	0.6844	1.060	666K	0.25
DRCN [13]		28.53	0.5547	0.973	30.37	0.6468	0.773	29.45	0.6780	1.013	112K	0.48
LapSRN [14]		28.68	0.5641	1.076	30.53	0.6541	0.813	29.65	0.6862	1.073	1305K	0.08
SESR [4]		28.70	0.5642	1.071	30.54	0.6575	0.823	29.66	0.6871	1.084	936K	0.35
CARN [1]		28.70	0.5676	1.092	30.56	0.6593	0.830	29.69	<b>0.6903</b>	1.094	1257K	0.04
RBAM (Ours)		<b>28.74</b>	<b>0.5683</b>	<b>1.104</b>	<b>30.59</b>	<b>0.6597</b>	<b>0.833</b>	<b>29.72</b>	0.6898	<b>1.099</b>	1252K	0.05

second and third rows also depict images that demonstrate RBAM’s ability to preserve cellular and vascular structure boundaries with proper sharpness for  $\times 4$  SR.

## 5 Conclusion

We proposed a novel network that leverages both 1<sup>st</sup>- and 2<sup>nd</sup>-order statistics for pooling in spatial and channel-wise attention mechanisms, resulting in a lightweight and fast model. We compared our proposed model with various traditional and DL-based SR techniques on three CLE datasets in terms of image quality assessment metrics, number of parameters and inference time. Despite small number of parameters, our RBAM network achieves competitive performance against existing lightweight methods across different datasets, downsampling factors, and SR performance evaluation criteria. Experimental

results also highlight the potential applicability of inexpensive software-based post-processing SR modules that improve degraded images in miniaturized CLE devices in real-time.

**Acknowledgments.** Thanks to the NVIDIA Corporation for the donation of Titan X GPUs used in this research and to the Collaborative Health Research Projects (CHRP) for funding.

## References

1. N. Ahn et al. Fast, accurate, and lightweight super-resolution with cascading residual network. In *ECCV*, 2018.
2. Y. Blau et al. The 2018 PIRM challenge on perceptual image super-resolution. In *ECCV Workshops*, pages 334–355, 2019.
3. F. Bray et al. Global cancer statistics 2018: GLOBOCAN estimates of incidence and mortality worldwide for 36 cancers in 185 countries. *CA: a cancer journal for clinicians*, 68(6):394–424, 2018.
4. X. Cheng et al. Sesr: Single image super resolution with recursive squeeze and excitation networks. In *IEEE ICPR*, pages 147–152, 2018.
5. C. Dong et al. Image super-resolution using deep convolutional networks. *IEEE TPAMI*, 38(2):295–307, 2016.
6. Z. Gao et al. Global second-order pooling neural networks. *arXiv:1811.12006*, 2018.
7. E. Grisan et al. 239 computer aided diagnosis of barrett’s esophagus using confocal laser endomicroscopy: Preliminary data. *Gast. Endosc.*, 75(4):AB126, 2012.
8. J. Hu et al. Squeeze-and-excitation networks. In *IEEE CVPR*, 2018.
9. J. Huang et al. Single image super-resolution from transformed self-exemplars. In *IEEE CVPR*, pages 5197–5206, 2015.
10. S. Izadi et al. Can deep learning relax endomicroscopy hardware miniaturization requirements? In *MICCAI 2018*, pages 57–64, 2018.
11. R. Kiesslich et al. Confocal laser endoscopy for diagnosing intraepithelial neoplasias and colorectal cancer in vivo. *Gastroenterology*, 127(3):706–713, 2004.
12. J. Kim et al. Accurate image super-resolution using very deep convolutional networks. In *IEEE CVPR*, pages 1646–1654, 2016.
13. J. Kim et al. Deeply-recursive convolutional network for image super-resolution. In *IEEE CVPR*, pages 1637–1645, 2016.
14. W. Lai et al. Fast and accurate image super-resolution with deep laplacian pyramid networks. *IEEE TPAMI*, pages 1–1, 2018.
15. R. W. Leong et al. In vivo confocal endomicroscopy in the diagnosis and evaluation of celiac disease. *Gastroenterology*, 135(6):1870 – 1876, 2008.
16. D. Ravi et al. Effective deep learning training for single-image super-resolution in endomicroscopy exploiting video-registration-based reconstruction. *International Journal of Computer Assisted Radiology and Surgery*, 13:917–924, 2018.
17. D. Rav et al. Adversarial training with cycle consistency for unsupervised super-resolution in endomicroscopy. *Medical Image Analysis*, 53:123 – 131, 2019.
18. D. Ștefănescu et al. Computer aided diagnosis for confocal laser endomicroscopy in advanced colorectal adenocarcinoma. *PloS ONE*, 11(5):e0154863, 2016.
19. R. Timofte et al. Anchored neighborhood regression for fast example-based super-resolution. In *IEEE ICCV*, pages 1920–1927, 2013.



20. R. Timofte et al. A+: Adjusted anchored neighborhood regression for fast super-resolution. In *ACCV*, pages 111–126, 2015.
21. Z. Wang et al. Image quality assessment: from error visibility to structural similarity. *IEEE TIP*, 13(4):600–612, 2004.